Annealing Characteristics of Ultrafine Grained Low-Carbon Steel Processed by Differential Speed Rolling Method

KOTIBA HAMAD and YOUNG GUN KO

The annealing behavior of ultrafine grained ferrite in low-carbon steel (0.18 wt pct C) fabricated using a differential speed rolling (DSR) process was examined by observing the microstructural changes by electron backscatter diffraction and transmission electron microscopy. For this purpose, the samples processed by 4-pass DSR at a roll speed ratio of 1:4 for the lower and upper rolls, respectively, were annealed isochronally at temperatures ranging from 698 K to 898 K (425 °C to 625 °C) for 1 hour. The deformed samples exhibited a complex microstructure in the ferrite phase consisting of an equiaxed structure with a mean grain size of ~0.4 μm and a lamellar structure with a mean lamellar width of ~0.35 μm. The texture evolved during deformation was characterized by the rolling and shear components with specific orientations. After annealing at temperatures lower than 798 K (525 °C), the aspect ratio of the deformed grains tended to shift toward a unit corresponding to the equiaxed shape, whereas the grain size remained unchanged as the annealing temperature increased. At temperatures above 798 K (525 °C), however, some grains with a low dislocation density began to appear, suggesting that the starting temperature of static recrystallization in the severely deformed ferrite grains was 798 K (525 °C). The annealing texture of the present sample after heat treatment showed a uniform fiber texture consisting of α- and γ-components.

I. INTRODUCTION

ULTRAFINE-GRAINED metals with a mean grain size less than 1 μm have been found to show superior mechanical properties, such as excellent strength and high ductility at low temperatures and/or high strain rates as compared to their coarse-grained counterparts.[1] Thermo-mechanical processing is generally used to achieve small grain sizes, but this approach generally fails to achieve a grain size smaller than 1 μm. Nevertheless, ultrafine-grained metals are produced effectively in the bulk dimensions using severe plastic deformation (SPD) methods where the processed material is subjected to intense plastic deformation, leading to significant refinement of the microstructure.[1,2] A range of SPD techniques have been developed to fabricate bulk ultrafine-grained materials, including equal-channel angular pressing (ECAP),[3–6] high-pressure torsion (HPT),[7] accumulative roll-bonding (ARB),[8] and differential speed rolling (DSR).[9,10] Langdon[11] reported that deformation by SPD could introduce a high density of dislocations, which would be rearranged to produce an array of grain boundaries, leading to the formation of ultrafine-grained structures.

Among the SPD methods, the DSR process is a promising method with potential for the continuous production of large bulk materials in the form of sheets for industrial applications. In this process, intense plastic deformation can be introduced uniformly throughout the sheet thickness through two identical working rolls that rotate at different roll speeds. Processing by the DSR method has been reported for several pure metals, such as Mg,[12–14] Al,[15,16] Cu,[17–19] Ti,[20,21] and steel.[22–27] These studies showed that significant grain refinement and improved mechanical properties could be achieved after DSR deformation under a range of processing conditions. To date, most studies have described the changes in microstructure and mechanical properties of the single-phase metals fabricated by DSR, but a little attention has been paid to multi-phase metals. Recently,[25] low-carbon steel (LCS) samples containing ferrite grains and pearlite colonies were fabricated successfully by DSR. The microstructural and textural evolutions were examined with respect to the number of DSR operations. The microstructure in the ferrite phase evolved to an ultrafine-grained microstructure after 4-pass DSR. In addition, cementite plates in the pearlite colonies were almost fully fragmented after 4-pass DSR at room temperature. The orientation distribution function (ODF) sections of the DSR-deformed samples revealed a gradual evolution of fiber textures with increasing number of DSR operations.

KOTIBA HAMAD, Assistant Professor, is with the School of Advanced Materials Science and Engineering, Sungkyunkwan University, Suwon 440-746, South Korea. YOUNG GUN KO, Associate Professor, is with the Plasticity Control & Mechanical Modeling Lab, School of Materials Science and Engineering, Yeungnam University, Gyeongsan 38541, South Korea. Contact e-mail: younggun@ynu.ac.kr

Ultrafine-grained metals processed by SPD are often annealed to ensure the thermal stability of these materials. This study examined the annealing behavior of LCS sample with ultrafine-grained structures fabricated by DSR.[25] In terms of the annealing behavior of ultrafine-grained LCS materials, several papers reported the annealing behavior of these materials after SPD deformation. Park et al.[28] examined the thermal stability of LCS (0.15 wt pct C) processed by ECAP. They reported that subsequent annealing after ECAP deformation at temperatures ranging from 673 K to 773 K (400 °C to 500 °C) resulted in the stable ultra-fine-grained structures with limited grain growth. Maier et al.[29] reported similar results where the thermal stability of ECAP-processed LCS containing 0.09 wt pct C was investigated. Therefore, the annealing behavior of the LCS materials with ultrafine-grained structures is available only on samples fabricated by multiple passes of ECAP deformation. In addition, despite the considerable activity in this field, information on the textural evolution of ultrafine-grained LCS during heat treatment was limited compared to the microstructural evolution and mechanical properties. In view of these deficiencies, the present study examined the effects of annealing on the microstructure and texture evolution of LCS fabricated by the DSR process.

II. EXPERIMENTAL PROCEDURES

Low-carbon steel (LCS) sheet, whose chemical composition was Fe-0.18 pct C-0.012 pct Si-0.5 pct Mn-0.007 pct Cr, was used. After machining into plates, 70 mm in length, 30 mm in width, and 4 mm in thickness, the material was homogenized at 1373 K (1100 °C) for 3 hours followed by furnace cooling to obtain an equiaxed microstructure with a grain size of ~100 μm, as shown in Figure 1(a). The equiaxed microstructure of LCS consisted of ~20 vol pct pearlite with remainder ferrite. A series of lubricated-DSR processes were carried out on the samples at room temperature using two identical rolls, 220 mm in diameter, at a roll speed ratio of 1:4 for the lower and upper rolls, respectively (Figure 1(b)), with the velocity of the lower roll fixed to 5 RPM. The samples were subjected to a 30-pct thickness reduction per pass, with an overall ~75-pct thickness reduction after 4-pass DSR. The deformed samples showed no obvious deformation failure, such as cracking or severe bending. The DSR-fabricated samples with a final thickness of ~1 mm can be used for sheet-metal forming processes, such as bending and stretch forming.[21]

The samples for isochronal annealing were covered by stainless steel foil to minimize decarburization. Annealing was carried out at 698 K to 898 K (425 °C to 625 °C) for 1 hour with a 50 K difference between test temperature, and the temperature was controlled within ±2 K during annealing. Transmission electron microscopy (TEM, Philips TECNAI G2 F20) of the deformed and annealed samples was carried out at an acceleration voltage of 200 kV. For the TEM observations, thin foils samples of LCS were fabricated by focused ion beam
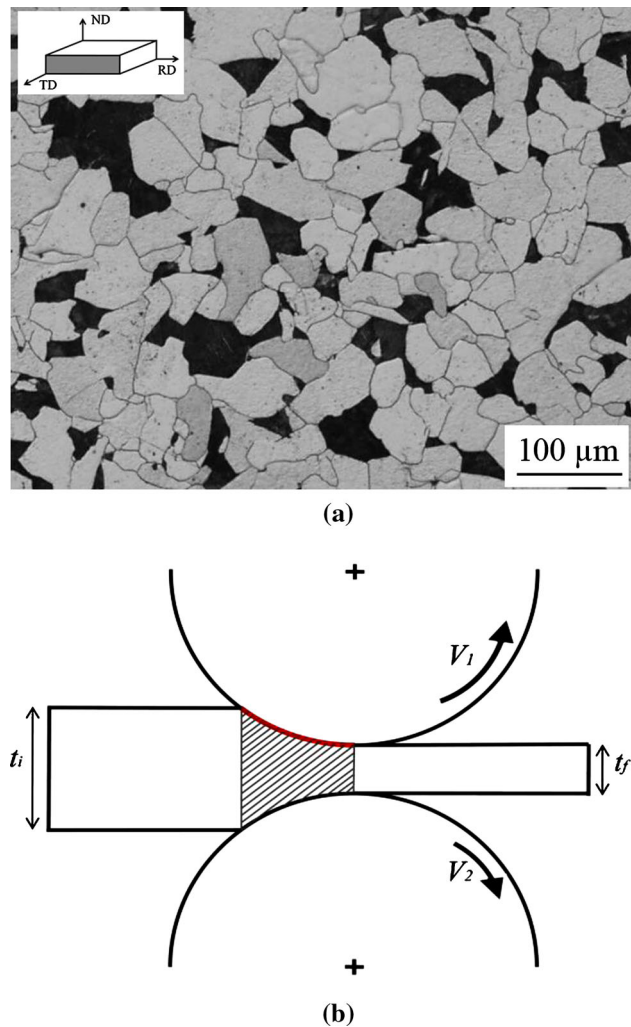

(a)

(b)

Fig. 1—(a) Initial microstructure of coarse-grained LCS (b) Schematic diagram of the DSR frame.

(FEI, Quanta 3D FEG) thinning. The microstructural and crystallographic features of the LCS samples were examined by electron backscatter diffraction (EBSD) in a scanning electron microscope with a field-emission gun (Hitachi S-4300 FESEM). The data were analyzed using a TSL OIM 6.1.3 software. Sheets cut from the rolling direction–normal direction (RD–ND) plane of the fabricated samples for EBSD analysis were polished mechanically and etched in a 2 pct solution of picric acid in ethanol. Because the pearlite colony, which is composed of fine lamellae of ferrite and cementite, does not provide a good pattern due to the overlapping of patterns from two different phases in the colony (ferrite and cementite), EBSD analysis was performed only on the ferrite grains after partitioning the data related to the pearlite colonies.[25] EBSD scans at high magnifications were obtained using step size of 0.02 μm. This step size was suitable for accurate grain boundaries analysis. The grain boundary distribution was evaluated under the assumption of a 2 to 15 deg misorientation angle for low-angle boundaries (LABs) and above 15 deg for high-angle boundaries (HABs). The grain shape aspect ratios were described as the grain diameter along ND

divided by the diameter along RD. For texture evolution, the data from the EBSD experiments were analyzed by the orientation distribution functions (ODF) calculated using a Harmonic Series Expansion method. The analysis was carried out in an Euler angle space (φ_1 = 0 to 90 deg, Φ = 0 to 90 deg, and φ_2 = 45 deg) using the non-orthonormal sample symmetry. The fraction of HABs, boundary misorientation distributions, grains size distributions, grain shape aspect ratio distributions, and texture obtained from the EBSD data were averaged over at least three maps including ~400 grains.

The LCS samples with mirror-like polished surfaces were examined using a Vickers microhardness tester equipped with a Vickers indenter with a load of 200 g and a dwell time of 10 seconds. The microhardness of the samples was recorded in the ferrite phase across the thickness direction (at least 20 measurements were conducted for each sample, which were used to calculate the mean values and standard deviations).

III. RESULTS

A. Deformed Samples

1. Microstructure

Previous studies examined the effects of the height reduction per pass on the microstructure homogeneity of steel samples.[26] The results showed that at a high speed ratio of 1:4 and a height reduction of 50 pct per pass, the ultrafine-grained grains with a uniform distribution would be achieved through the thickness of the deformed samples after 2-pass DSR. Accordingly, the DSR deformation conditions used in this study could provide reasonable homogeneous distributions of the grain size through the thickness of the LCS sample. Figure 2 presents the microstructural evolution of the ferrite phase in the LCS sample after 4-pass DSR deformation at a roll speed ratio of 1:4 and height reduction of 30 pct per pass. As shown in Figure 2, after DSR deformation, two types of characteristic ultrafine-grained structures were observed in the ferrite phase, *i.e.*, a lamellar structure with a mean boundary interval of ~0.35 μm (Figure 2(a)) and equiaxed grained structure with a mean size of ~0.4 μm (Figure 2(b)). In general, the mean grain size, which is the key parameter in defining the nature of the ultrafine-grained structure achieved after SPD deformation, was determined from the measurements taken by TEM. On the other hand, these measurements tend to be difficult in cases where many grain boundaries in the SPD-deformed materials are diffused in nature or represent the transition zones between highly deformed grains.

The problem of microstructural characterization can be handled significantly by EBSD. Figure 3(a) shows the inverse pole figure (IPF) map taken from the ND–RD plane of the DSR-deformed LCS sample. The stereographic triangle in Figure 3(a) shows the orientations of the individual grains recorded by EBSD. On the other hand, an analysis of the microstructural evolution by EBSD can introduce an ancillary problem associated
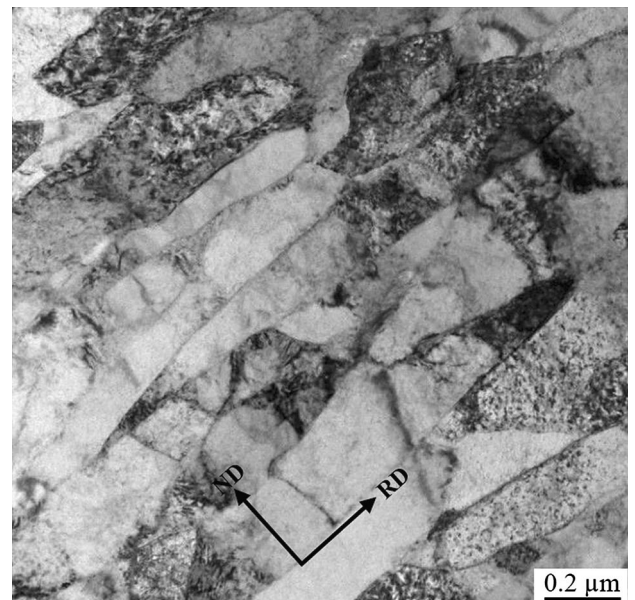
(a)
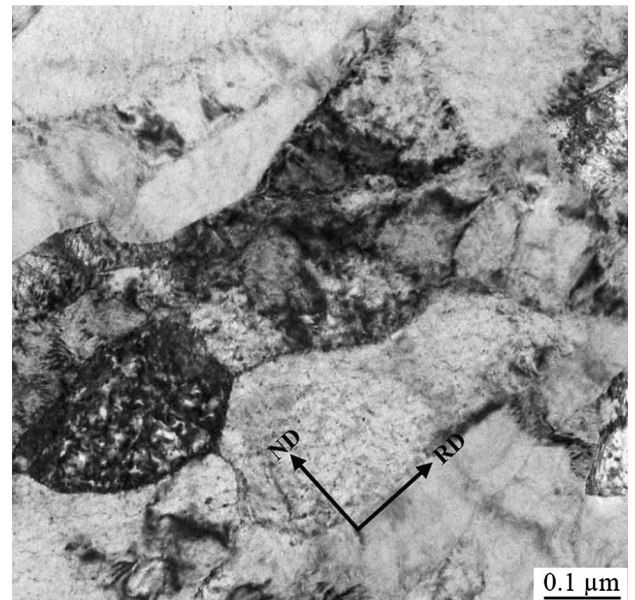
(b)

Fig. 2—TEM images showing the complex microstructure obtained for the LCS samples after processing by DSR for 4 passes.

with the appropriate tolerance angle (TA). The TA is defined as a parameter of the EBSD measurements in that two neighboring points are considered to belong to the same grain if the difference in their individual misorientations is less than the TA. Figure 3(b) shows the effect of using different TA values, where the grain size distributions are shown for the sample processed by DSR using two different TA values, 2 and 15 deg, which represent the lower and upper limits of the low-angle grain boundaries, respectively. In general, the grain size distribution after DSR deformation appeared to be smooth, as shown in Figure 3(b). In addition, the grain size was larger when using a TA of 15 deg compared to that of the grain size determined at a TA of 2 deg.
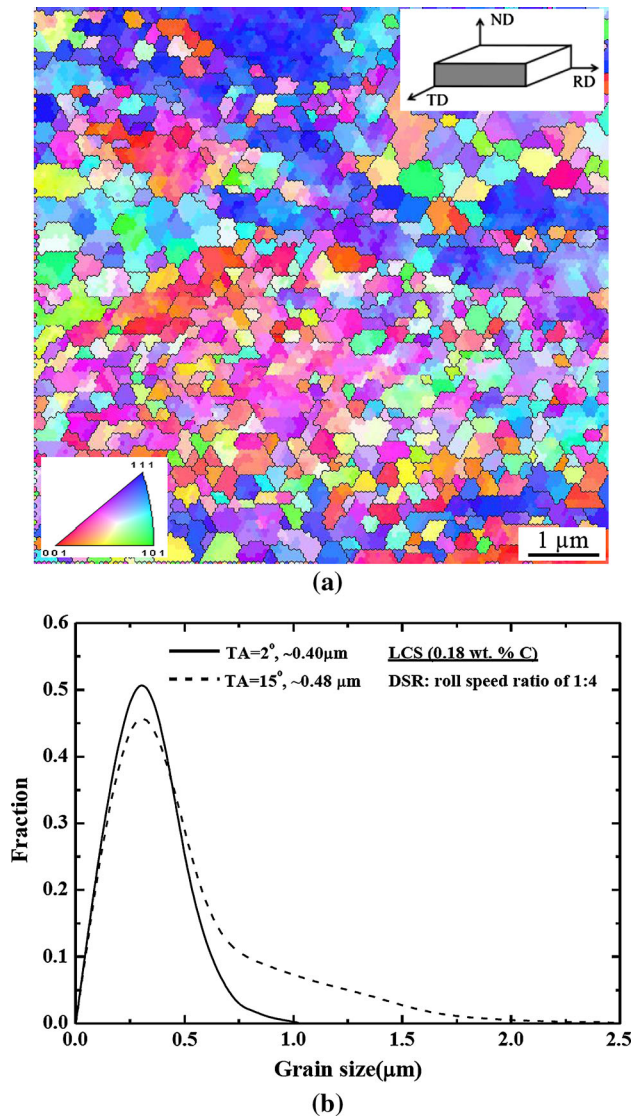
Fig. 3—(a) Inverse pole figure (IPF) and (b) grain size distribution of the LCS samples after processing by DSR for 4 passes.

Furthermore, the grain size distribution at TA = 2 deg was uniform (Figure 3(b)). Therefore, the grain sizes reported in this paper were recorded using EBSD, and corresponded to TA = 2 deg.

The IPF map in Figure 3(a) reveals complicated deformation microstructures consisting of elongated grains in the rolling direction surrounded by ultrafine grains. An earlier study[25] reported that the formation of ultrafine grains located along the high-angle boundaries of the elongated grains (called "necklace-like" structure) is the result of a strain-induced recrystallization process (continuous dynamic recrystallization). In this process, the subgrained structures formed at a low level of deformation within the elongated grains change into ultrafine grains with increasing level of strain imposed due to the coalescence of subgrains. On the other hand, Hughes and Hansen[30] proposed an alternative mechanism of structural refinement during the cold rolling of pure nickel. They reported that at a low level of deformation, the initial microstructure evolved

into subdivided structures composed of small cells arranged in blocks that were surrounded by dislocation walls, leading to the formation of different textural components within the initial grains. With increasing imposed strain, the structure underwent a further transformation, which included the formation of fine grains with strong rolling texture orientations. Therefore, the IPF map presented in Figure 3 confirms the formation of the ultrafine-grained structures after DSR deformation.

2. *Texture*

To examine the effects of the deformation by DSR on the texture evolution of the deformed sample, two types of textures were considered. The rolling texture, which is defined as the sum of the four different texture components: {001}⟨110⟩, {112}⟨110⟩, {111}⟨110⟩, and {111}⟨112⟩, and the shear texture consisting of components with orientations of {110}⟨001⟩, {110}⟨112⟩, and {112}⟨111⟩. Figure 4(a) presents the fiber characterization and textural components of bcc materials found in the orientation distribution function (ODF) sections of Euler space when φ_2 = 45 deg. The calculated ODF depicted from the orientation maps of the DSR-deformed sample is shown in the φ_2 = 45 deg section of the Euler space (Figure 4(b)).

As shown in Figure 4(b), the texture evolved LCS sample after 4-pass DSR consisted of strong components with rolling orientations, such as {001}⟨110⟩ and {112}⟨110⟩, along with a weak shear texture component with {110}⟨001⟩ orientation (Goss) was also observed. Because the deformation mode in asymmetric rolling is approximated by the superposition of a plane strain and a simple shear in the rolling direction, the deformation by DSR resulted in more complex textural distributions through the thickness compared to those achieved after equal speed rolling (ESR). For example, the appearance of the Goss component in the DSR-deformed sample was associated with the asymmetrical rolling mode and the impact of the shear component can increase with increasing roll speed ratio.[31] In addition, rolling texture components, such as {111}⟨110⟩ and {111}⟨112⟩, were observed in the LCS sample processed by 4-pass DSR, indicating plane strain deformation. After ESR deformation, shear texture components form in the surface layer of the ESR-deformed sample because of the high level of friction between the roll and sample surface,[32] whereas components with rolling texture orientations form in the middle layer due to plane strain deformation.[32] The change in the deformation mode from the shear deformation concentrated at the surface to the plane strain deformation in the middle thickness can result not only in an inhomogeneous microstructure, but also in a texture gradient through the thickness in the ESR-processed materials. Raabe[33] reported that the texture components developed as a result of shear deformation in the surface during ESR become progressively weaker with depth. In the DSR process, however, shear deformation is not only the result of friction between the roll and sample surface, but also due to asymmetry in rolling mode. Chen[34] examined the effects of the roll speed ratio on the texture
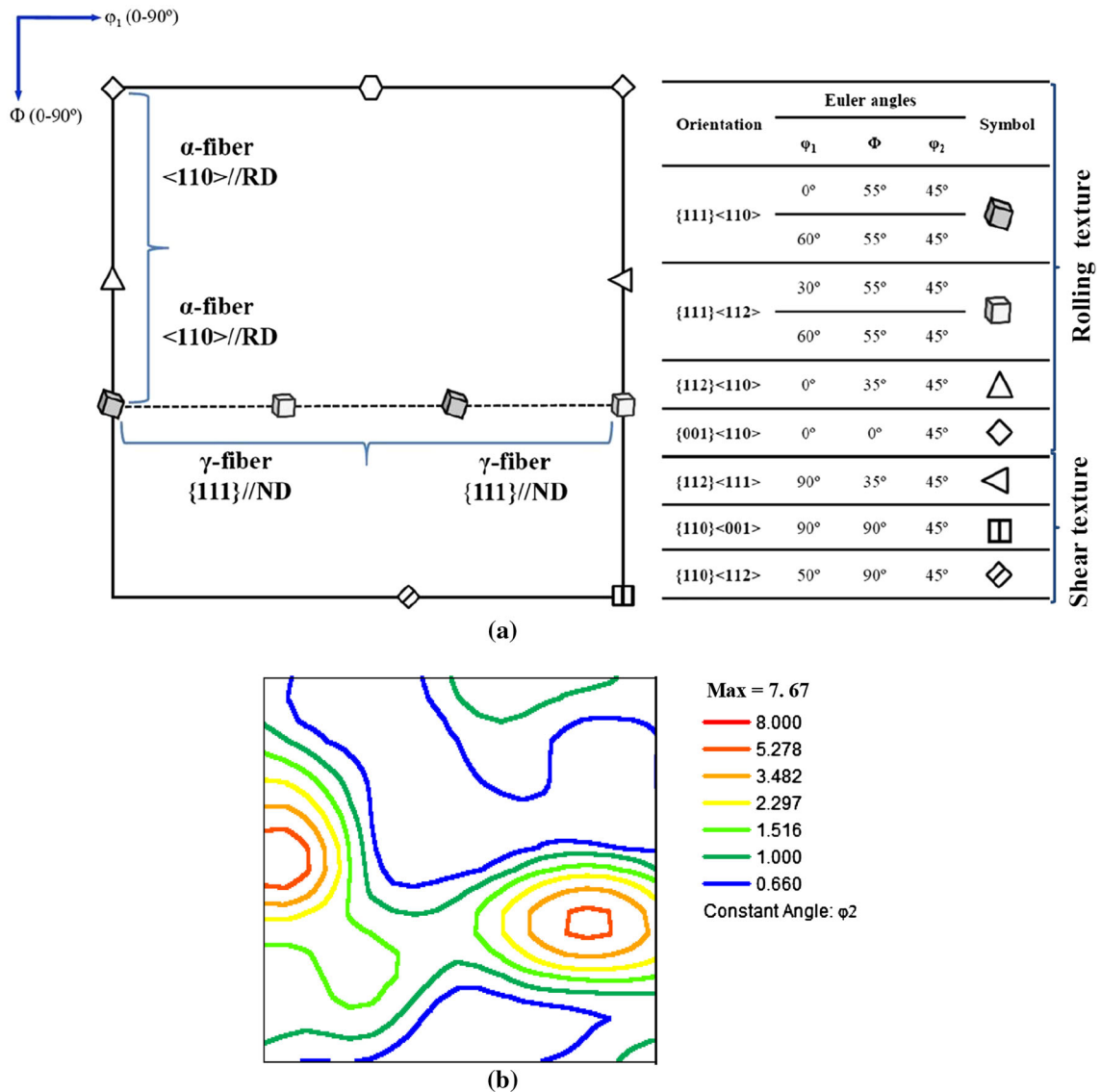
Fig. 4—(*a*) Fiber characteristics and texture components of bcc materials found in the orientation distribution function (ODF) sections of the Euler space when $\varphi_2 = 45$ deg. (*b*) ODF sections at $\varphi_2 = 45$ deg for the LCS after processing by DSR for 4 passes.

components distribution through the thickness of AA1050 alloys processed by DSR. They found that at roll speed ratios higher than 2, the texture components that developed in the middle layer were similar to those developed in the surface layer, suggesting a homogenous distribution of texture components through the thickness of the DSR-deformed sample. In the present study, a high roll speed ratio of 1:4 was applied to achieve homogenous evolution of the texture components through the thickness of the deformed sample.

B. *Annealed Samples*

1. *Microstructure*

Figures 5 and 6 present the microstructural evolution and the changes in the associated microstructural parameters of the DSR-deformed LCS samples annealed for 1 hour at various temperatures. The EBSD maps in Figure 5 reveal gradual and uniform collapse of

the lamellar structure with the concomitant evolution of equiaxed grains. After annealing at 748 K and 798 K (475 °C and 525 °C), the mean grain size (*D*) increased from ~0.8 *μ*m to ~3.5 *μ*m, respectively. At 748 K (475 °C), however, local regions of the microstructure still retained the lamellar-like morphology achieved initially after DSR deformation. Details of the annealed microstructures showed that the grain aspect ratio distributions shifted toward grains with an almost equiaxed shape as the annealing temperature was increased, as shown in Figure 6(a). This suggests that both the uniform coarsening and evolution of a more equiaxed grain configuration occurred in the DSR-deformed samples during the present annealing treatment. Uniform coarsening behavior with a grain size of 0.8 *μ*m was evident in the other regions of the sample annealed at 748 K (475 °C) compared to the samples after DSR deformation. Figure 6(c) presents the lognormal (L–N) probability distribution used to examine the coarsening
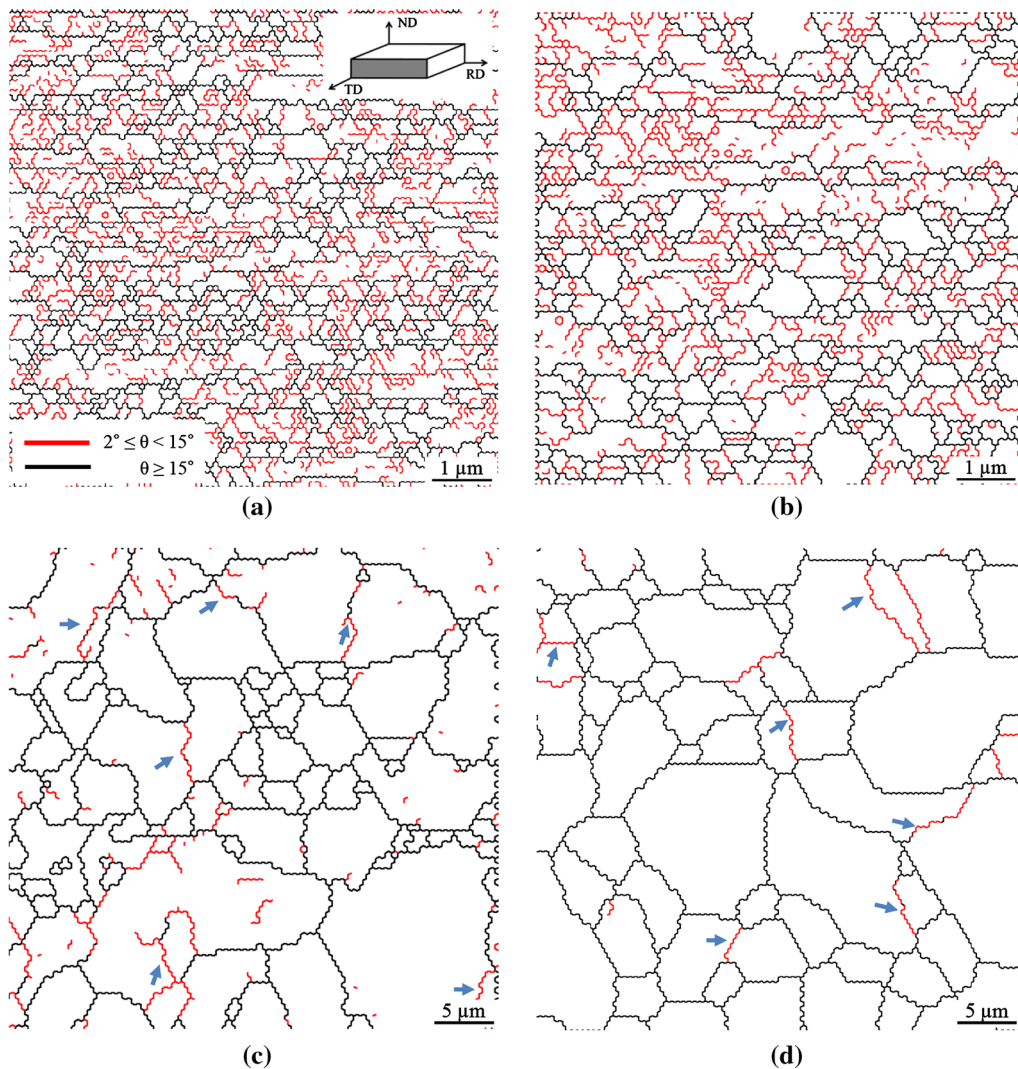
Fig. 5—Representative EBSD grain boundary maps of the DSR-deformed LCS samples after isochronal annealing for 1 h at (*a*) 748 K (475 °C) (*b*) 798 K (525 °C) (*c*) 848 K (575 °C) (*d*) 898 K (625 °C).

behavior of the DSR-deformed LCS samples during annealing. The recent grain coarsening study by Ferry and Burhan[35] on an Al-0.3 pct Sc alloy showed that the L–N distribution function can be used to gain a more fundamental understanding of the normal grain coarsening behavior in polycrystalline materials compared to other continuous probability distributions, such as the Rayleigh and Gamma distributions. As shown in Figure 6(c), the peaks for the L–N distribution function shifted to the right with increasing annealing temperature, showing invariant coarsening behavior in the range of annealing temperatures used in the present study.[36] In addition, the L–N distribution retained a good fit for the data even after annealing at 898 K (625 °C), confirming the uniformity of the coarsening observed in the EBSD maps presented in Figure 5. Figure 6(d) shows the distribution of grain boundaries misorientations of the annealed samples. The fraction of HABs evolved during annealing of the DSR-deformed samples increased slightly with increasing annealing temperature. After annealing at 748 K (475 °C), the dislocations

generated by DSR deformation could be absorbed at the grain boundaries with a concomitant increase in the misorientation angles. After annealing at 798 K (525 °C), however, the low-angle boundaries still remained within the deformed grains because some dislocations were not absorbed during recovery. In addition, the fraction of LABs observed in the samples after annealing at 848 K and 898 K (575 °C and 625 °C) contributed to the formation of coarse grains with high-angle boundaries, as indicated by the arrows in Figures 5(c) and (d).

2. *Microhardness*

Figure 7 represents the dependence of the annealing temperature on the average microhardness, softened fraction and stored energy in DSR-deformed LCS. The evolution of the mechanical properties during annealing was in good agreement with the kinetics responsible for grain growth during annealing. The as-deformed samples with a grain size of ~0.4 μm and a microhardness of ~252 Hv showed high thermal stability up to 748 K (475
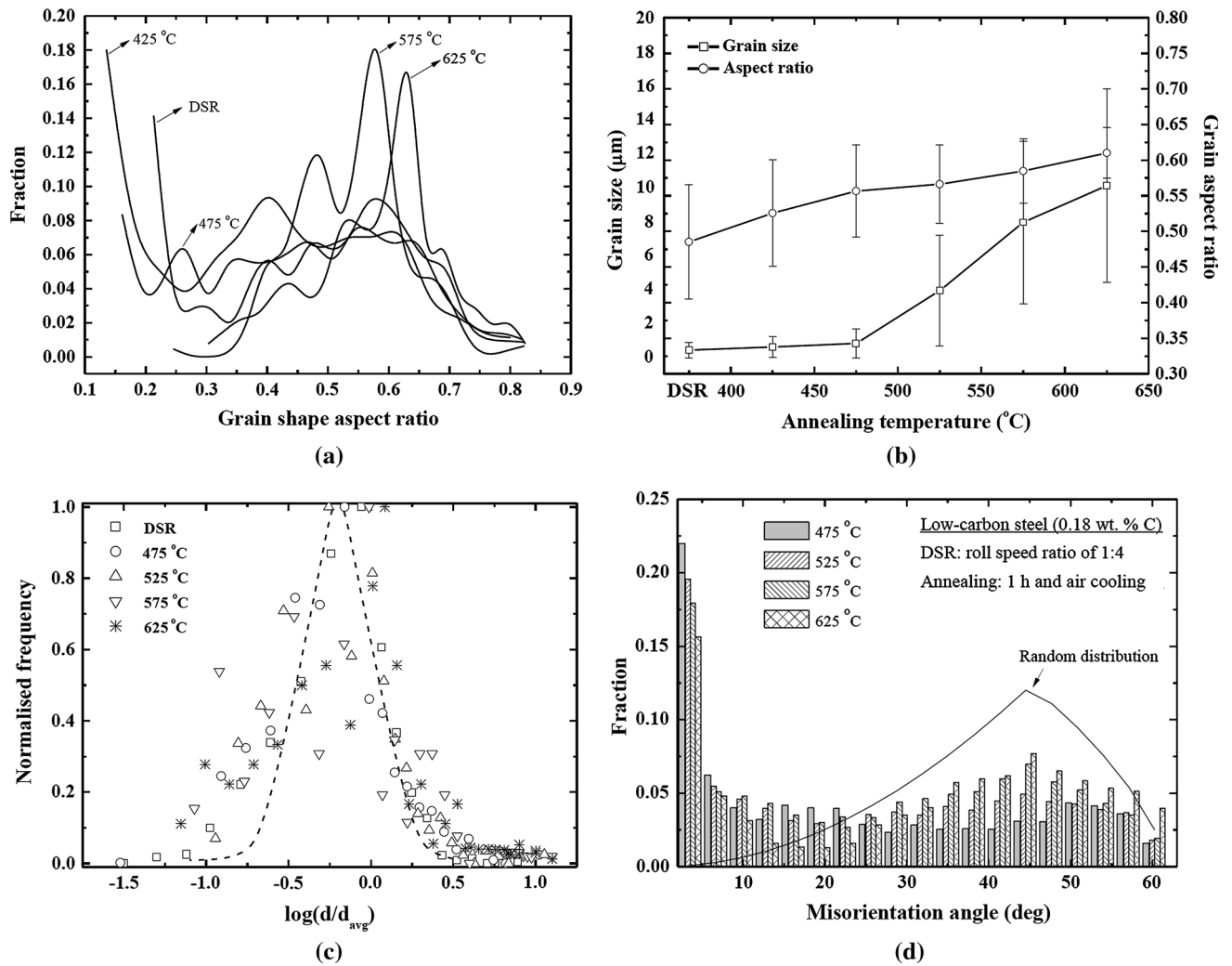
Fig. 6—Microstructural parameters of the DSR-deformed LCS samples during annealing (*a*) grain shape aspect ratio distributions (*b*) grain size and aspect ratio (*c*) normalized grain size distributions (*d*) distribution of the grain boundaries misorientations (LABs and HABs).

°C), with a small decrease in microhardness, which is normally related to the recovery process occurring during the first stage of annealing. After annealing at 798 K (525 °C), the microhardness decreased to 195 Hv, showing grain growth with a size of ~3.5 μm. This decrease became pronounced with increasing annealing temperature after 848 K and 898 K (575 °C and 625 °C). The softened fraction (*X*) can also be expressed in terms of the microhardness as follows:[36,37]

$$X = \frac{H_d - H_t}{H_d - H_0} \qquad [1]$$

where H_d, H_t, and H_0 are the microhardness after DSR deformation, the instantaneous microhardness at time *t*, and the microhardness of the initial sample prior to DSR, respectively. The softened fraction was related to the decreasing tendency of microhardness due to annealing heat treatments. Thus, this concept was correlated to a fraction of the recrystallized grains of the severely deformed materials.[38] Figure 7(a) presents the softened fraction as function of the annealing

temperature. After annealing the DSR-deformed LCS sample at 748 K (475 °C), the estimated softened fraction showed a ~2 pct reduction compared to the as-deformed sample (as indicated by the arrow in Figure 7(a)). In addition, the samples annealed at 798 K, 848 K, and 898 K (525 °C, 575 °C, and 625 °C) showed a softened fraction of ~37, 85, and 87 pct, respectively. The stored energy (E_d), which is a measure of the internal misorientations and dislocation density, was calculated from the microhardness in a simple equation as follows:[38]

$$E_d = \rho E = \frac{1}{18G}\left(\frac{H_t - H_0}{M\alpha}\right) \qquad [2]$$

where ρ is the total dislocation density, *E* is the line energy of the dislocations, *M* is the Taylor factor of bcc materials (3.05), α is a constant (0.3), and *G* is the shear modulus of the LCS materials (79 GPa). The stored energy can also be calculated using the data from EBSD analysis,[39] but the applicability of EBSD for calculating the stored energy has some limitations because of the
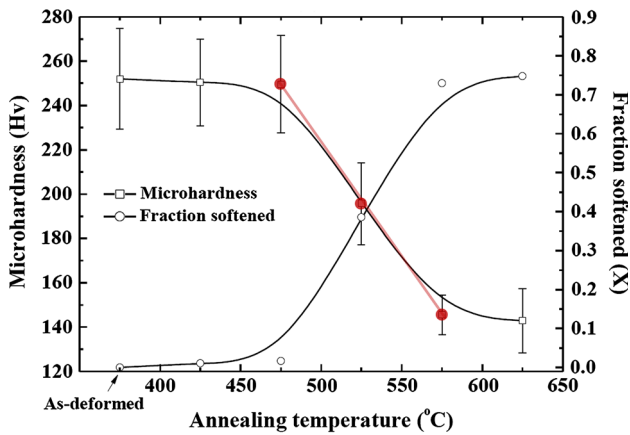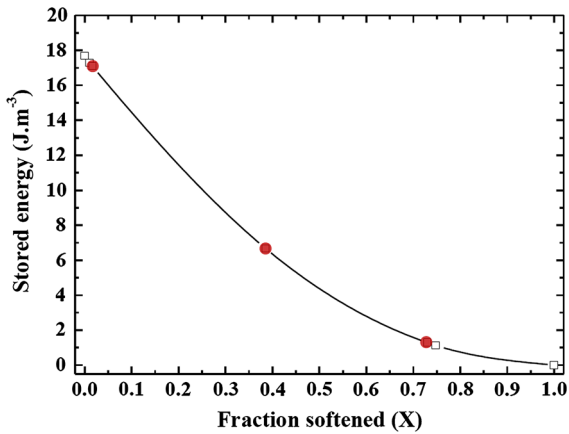
Fig. 7—(a) Microhardness and softened fraction as function of the annealing temperature for 1 h and (b) stored energy in the annealed samples as function of the softened fraction.

statistically stored dislocations that cannot be accounted for through EBSD. On the other hand, the microhardness is a reflection of the total dislocation density and includes the stored energy contribution from the statistically stored dislocations. Figure 7(b) presents the stored energy in the DSR-deformed samples during annealing as a function of the softened fraction determined from the microhardness measurements (Figure 7(a)). As shown in Figure 7(b), the stored energy decreased with increasing annealing temperature, and a sharp decrease in stored energy was observed after annealing at 798 K (525 °C), indicating a large reduction of the total dislocation density. In addition, the stored energy of the samples annealed at 698 K and 748 K (425 °C and 475 °C) was released to a certain degree due the relaxation of internal stresses by the recovery process.[40]

3. Texture

The φ_2 = 45 deg section of the Euler orientation space by plotting the measured ODFs (Figure 8) shows the dependence of the texture evolution of the DSR-deformed LCS samples on the annealing temperature. The results presented in Figure 8 show that the annealing texture of the DSR-deformed LCS samples also showed fiber textures, consisting of components with α-fibers:

{001}⟨110⟩, {112}⟨110⟩ and γ-fiber: {111}⟨110⟩ and {111}⟨112⟩. On the other hand, the fiber textures obtained during annealing were more uniform than those obtained after DSR deformation (Figure 4(b)), and the uniformity of the γ-fiber increased gradually with increasing annealing temperature. In the ODFs obtained from the samples annealed at 848 K and 898 K (575 °C and 625 °C), the γ-fiber lost some of its intensity, which concentrates around the α-fiber ({111}⟨110⟩). In addition, the maximum intensity of the texture measured in the samples decreased with increasing annealing temperature.

IV. DISCUSSION

A. Microstructure Stability of DSR-Deformed LCS

This paper reported the results of the microstructural evolution of LCS (0.18 wt pct C) deformed by the DSR process together with the microstructural changes occurring during annealing of the DSR-deformed LCS samples. Deformation after the 4-pass DSR led to a complex microstructure in the ferrite phase, consisting of a lamellar structure with a mean boundary interval of ~0.35 μm and an almost equiaxed grained structure with a mean size of ~0.4 μm. After annealing the DSR-deformed LCS samples, recovery occurred over the entire range of annealing temperatures between 698 K and 748 K (425 °C and 475 °C) for 1 hour (Figures 9(a) and (b)), leading to a slight decrease in microhardness compared to the as-deformed sample due to a decrease in dislocation density. At the same time, the aspect ratio of the grains tended toward a value of 1 for an equiaxed grain shape with a slight increase in size of 0.6 and 0.8 μm for the samples annealed at 698 K and 748 K (425 °C and 475 °C), respectively. Until such recovery is completed, the LCS samples had a duplex structure consisting of bands of ultrafine grains surrounded by elongated grains. At high annealing temperatures (≥798 K (525 °C)) for 1 hour, a second recrystallization process occurred, in that the ultrafine grains were replaced with larger grains (Figure 9(c)). The extremely fine grains with a size of ~0.1 μm (Figure 9(c)) at the grain boundaries suggested that the recovery was almost complete and recrystallization became active after annealing at 798 K (525 °C).

Park et al.[28] reported the annealing behavior of the LCS materials with ultrafine-grained structure in the ferrite phase. They examined the effects of heat treatments between 673 K and 873 K (400 °C and 600 °C) for 1 h on the microstructure and mechanical properties of the ECAP-deformed LCS samples containing 0.15 wt pct C. The results showed that the deformation of LCS materials by the 4-pass ECAP processes at 623 K (350 °C) would result in materials with high thermal stability and limited grain growth at annealing temperatures below ~773 K (500 °C). More recently,[29] ECAP-fabricated ultrafine-grained LCS materials (0.09 wt pct C) containing 0.08 wt pct Mo as a thermal stabilizer were annealed. The results showed that the materials fabricated after 6-pass ECAP deformations at 573 K (300 °C)
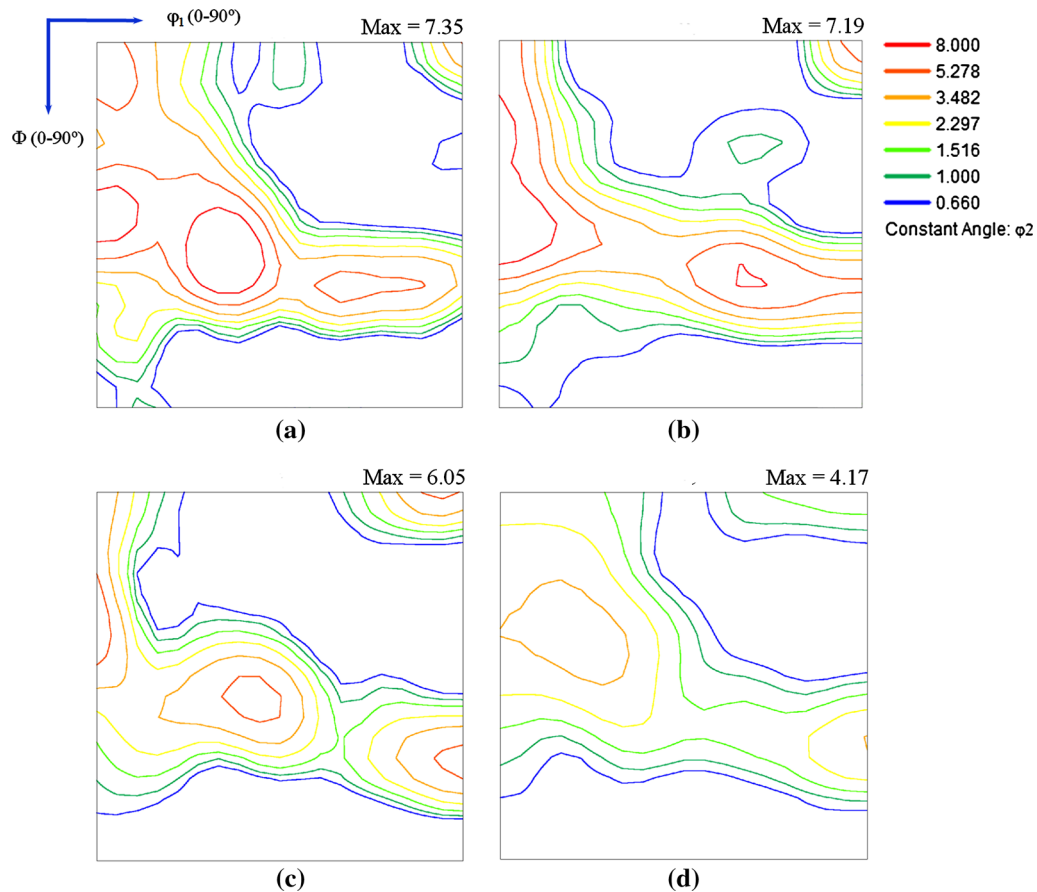
Fig. 8—Orientation distribution function (ODF) sections at φ_2 = 45 deg for the DSR-deformed LCS samples after isochronal annealing for 1 h at (*a*) 748 K (475 °C) (*b*) 798 K (525 °C) (*c*) 848 K (575 °C) (*d*) 898 K (625 °C).

possessed high thermal stability at temperatures up to 773 K (500 °C). In the present study, the processing of LCS (0.18 wt pct C) by 4-pass DSRs at room temperature led to thin sheet materials with a high thermal stability of ~773 K (500 °C), which was similar to that obtained in the LCS samples through multiple passes by ECAP at high deformation temperatures and in the presence of thermal stabilizers. Therefore, 773 K (500 °C) can be the upper temperature limit for DSR steel with an ultrafine-grained structure in industrial applications.

B. *Partitioning of Recrystallized Microstructure*

Partitioning of the recrystallized (RX) grains was performed on the samples annealed at 748 K, 798 K, and 848 K (475 °C, 525 °C, and 575 °C), which are denoted by the red symbols in Figures 7(a) and 7(b), to better understand the microstructural evolution and softening behavior of the LCS sample fabricated by the DSR during annealing. Different methods were suggested to distinguish the RX grains from the deformed matrix using the data from EBSD experiments. For example, the criterion of the grain size was used in one study to partition the RX grains in austenitic stainless steel samples forged at 1273 K (1000 °C).[41] On the other hand, this method could only be applied to

situations, where there is a distinct difference in grain size between RX and deformed grains. However, this method would be hard to be applicable in the case of grain growth. In addition, the image quality (IQ) was used because the recrystallized grains with less amount of dislocations inside them were believed to be superior to the deformed grains, but the IQ values of the grains could be affected by the surface preparation of the sample prior to the microstructural observation using EBSD.[42] In this study, partitioning of the microstructures to separate the recrystallized grains and deformed grains was performed using the criteria of the grain orientation spread (GOS), which was calculated from the average orientation for each grain, as shown in Figure 10. Similar analyses to partition the recrystallized grains from the deformed grains have been reported.[38,43] These analyses provided more effective separation between the various structural types in magnesium samples processed by asymmetrical rolling at different temperatures. Grains with orientation spread values higher than the average GOS value are considered to be deformed grains, whereas grains with orientation spread values lower than the average GOS value are considered to be recrystallized grains. The validity of partitioning was confirmed using the following two considerations: (i) The morphology of the RX grains should be more equiaxed with an aspect ratio
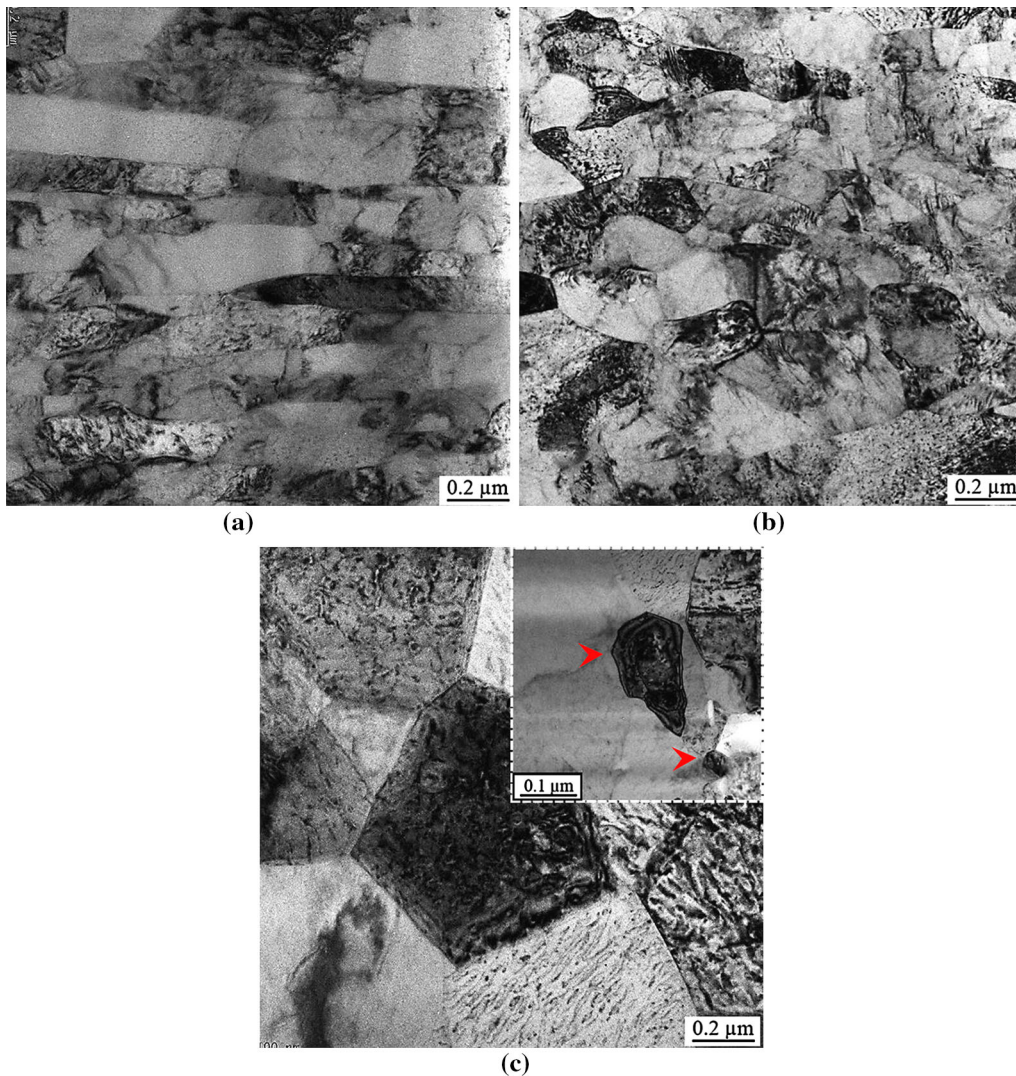
Fig. 9—TEM images of the DSR-deformed LCS samples after isochronal annealing for 1 h at (*a*) 698 K (425 °C) (*b*) 748 K (475 °C) (*c*) 798 K (525 °C).

close to 1, whereas the deformed grains should be more elongated (Figure 11(a)) (ii) The fraction of grain boundaries with a high angle of misorientations should be higher in the recrystallized microstructure than those in the deformed microstructure (Figure 11(b)).

Figure 12 presents EBSD maps of the DSR-deformed samples after annealing at 475 K, 525 K, and 848 K (202 °C, 252 °C, and 575 °C). Both the grain size and area fraction of the RX microstructures increased with increasing annealing temperature, where partial recrystallization corresponding to approximately ~23, ~31, and ~69 pct were recorded after annealing at 748 K, 798 K, and 848 K (475 °C, 525 °C, and 575 °C), respectively. In addition, the area fraction of large recrystallized grains increased with increasing annealing temperature and that of the small grains decreased, suggesting that the growth of large grains occurred at the expense of smaller grains. The area fraction of the RX microstructures during annealing might affect the softening behavior of the materials. Consequently, the lower microhardness of the samples annealed at 848 K (575 °C) (Figure 7(a)) reflected the existence of a larger fraction of recrystallized microstructures, as shown in Figure 12. On the other hand, the constant microhardness after annealing at 898 K (625 °C) suggested that the coarsening of recrystallized grains had a negligible effect on the microhardness at annealing temperatures of 848 K and 898 K (575 °C and 625 °C). This suggests that the softening behavior of the DSR-deformed sample during annealing would be affected dominantly by the area fraction of the recrystallized microstructures rather than by the coarsening of recrystallized grains.

C. Evolution of the Crystallographic Texture During Annealing

After deformation by the DSR process, the LCS sample exhibited strong fiber textures consisting of α-fibers and γ-fibers, which are typical of rolled ferritic steels.[26] After annealing, however, the strong fiber textures consisting of α-fibers and γ-fibers, which formed
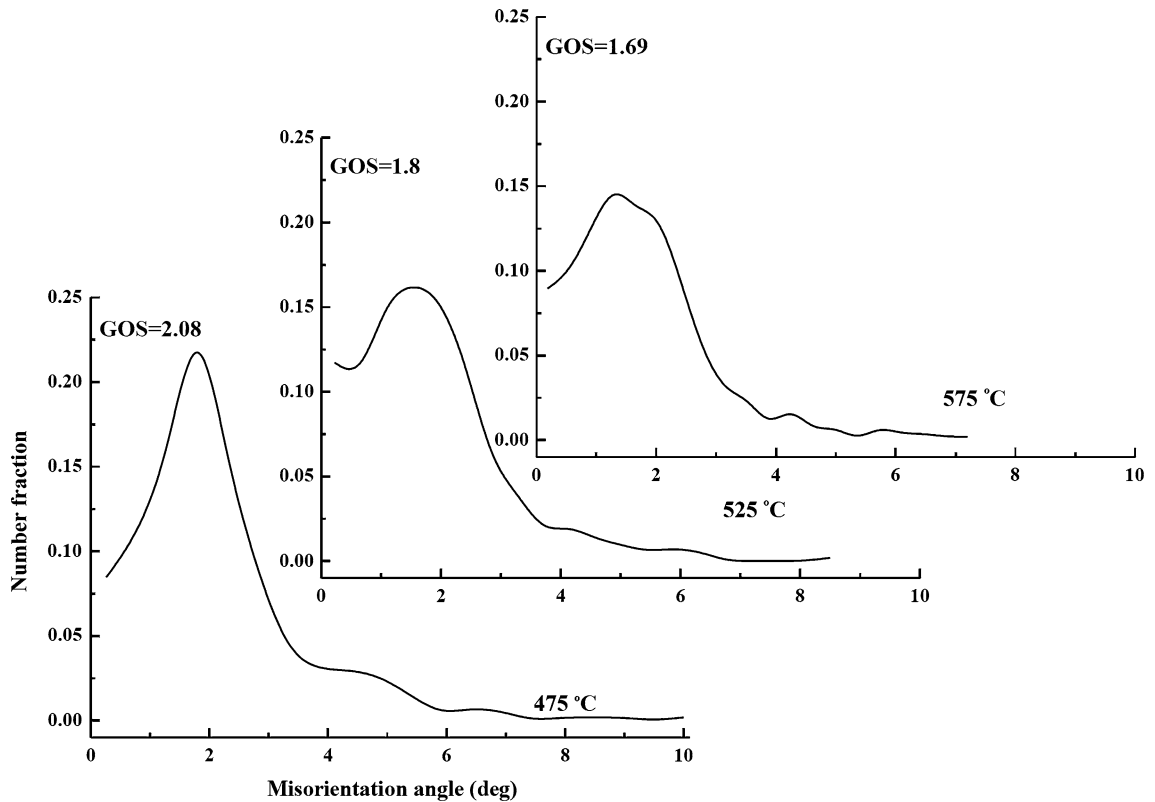
Fig. 10—Grain orientation spread (GOS) for the DSR-deformed LCS samples after isochronal annealing for 1 h at 748 K, 798 K, and 848 K (475 °C, 525 °C, and 575 °C).

after deformation by DSR, tended to become weaker and more uniform. This tendency increased gradually and became pronounced with increasing annealing temperature, as shown in Figure 8. In general, grains with the γ-fiber texture orientation obtained after DSR deformation can be consumed during annealing because of the high stored energy in the these grains. Figure 13 presents the variations in the prevalent fibers consisting of α-fibers and γ-fibers, which appeared in the DSR-deformed LCS samples during annealing.

As shown in Figure 13(a), the intensity of the rotated cube component ({001}⟨110⟩) increased after annealing compared to that of the deformed sample, whereas the intensity of the component with the {111}⟨112⟩ orientation (γ-fiber texture) decreased with increasing annealing temperature (Figure 13(b)). This can be attributed to the lower microstructural energy stored in α-fiber-oriented grains. Figure 14 presents the kernel average misorientation (KAM) maps to show the amount of stored energy in the texture components obtained in the LCS sample after DSR deformation. The KAM map is generally used to reveal the local misorientation and the amount of stored energy, and is calculated based on the degree of misorientation between a kernel (measuring point) and its neighbors. The γ-fiber-oriented grains exhibited large local misorientations (KAM ~1.5 deg), as shown in Figure 14(d), suggesting that these grains underwent severe deformation during DSR. On the other hand, the low KAM value (~0.6 deg) indicated that the amount of the stored

energy in the α-fiber-oriented grains is lower than that of the γ-fiber-oriented grains, as shown in Figures 14(a) and (b). From KAM maps presented in Figure 14, the grain with the highest KAM value shows {111}⟨112⟩ orientation, whereas the grain with the lowest KAM values shows a {001}⟨110⟩ orientation, as shown by the bcc unit cells constructed for the {001}⟨110⟩ and {111}⟨112⟩ orientations. Accordingly, grains with γ-fiber orientations, {111}⟨112⟩, would be consumed in the early stages of annealing according to their α-fiber neighbors, leading to a decrease in the intensity of components with γ-fiber orientations. This confirms that the local degree of misorientation is one of the important driving forces for grain growth and textural evolution during the annealing of the ultrafine-grained LCS samples fabricated by DSR.

Although the intensities of some components decreased after annealing, the deformation texture components remained the same during annealing, indicating the mechanism of continuous recrystallization.[44] Song et al.[45] reported this tendency, in which the intensity of components with γ-fiber orientations decreased during annealing treatment of steel materials. They examined the textural evolution during the annealing of ultrafine-grained low-carbon steel (0.22 wt pct C and 0.74 wt pct Mn) fabricated by a large-strain deformation. The results showed that the intensities of the components with orientations belonging to the γ-fiber decreased after annealing at 823 K (550 °C). In addition, a similar conclusion was reached in the tests on
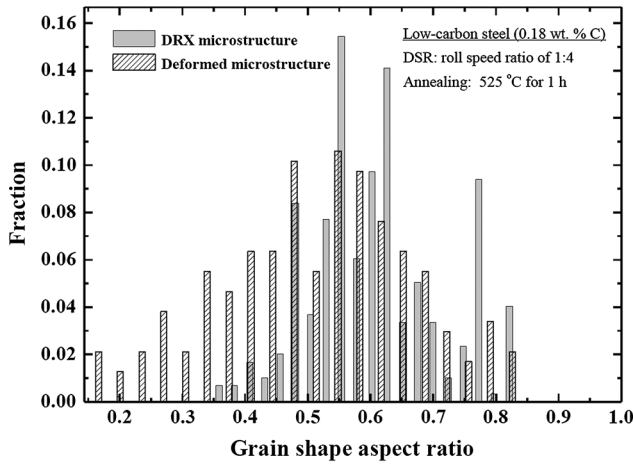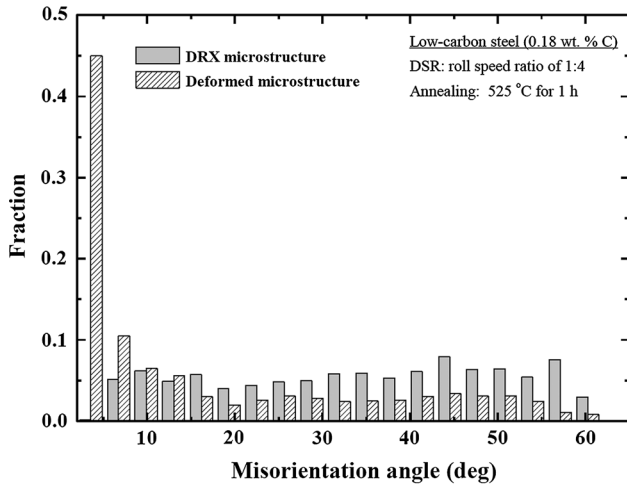
Fig. 11—(a) Grain aspect ratio distribution of RX microstructure and deformed microstructure in the DSR-deformed sample after isochronal annealing for 1 h at 798 K (525 °C) (b) grain boundaries misorientations distributions of RX microstructure and deformed microstructure in the DSR-deformed sample after isochronal annealing for 1 h at 798 K (525 °C).

medium-carbon steel samples (0.36 wt pct C) after a warm deformation process.[46] The intensities associated with the components belonging to γ-fiber decreased with increasing deformation temperature between 873 K and 983 K (600 °C and 710 °C).

D. Coarsening Behavior

The grain-coarsening behavior of the DSR-deformed LCS samples during annealing was discussed by comparing the arithmetic mean grain size (D) and standard deviation (σ) of the data with calculated values (D_c and σ_c), which were derived from the fitted lognormal distributions. D_c and σ_c were calculated using the following equations:[35]

$$D_c = \exp\left(\ln D_g + \frac{(\ln \sigma_g)^2}{2}\right) \quad [3]$$

$$\sigma_c = \sqrt{\exp\left(2\ln D_g + (\ln \sigma_g)^2\right)\left(\exp(\ln \sigma_g)^2 - 1\right)} \quad [4]$$

where D_g and σ_g are the geometric mean size and geometric standard deviation, respectively, which were calculated using the following equations:[35]

$$D_g = \exp\frac{\sum (N_i \ln D_i)}{\sum N_i} \quad [5]$$

$$\sigma_g = \exp\left[\frac{\sum N_i(\ln D_i - \ln D_g)^2}{\sum N_i}\right]^{0.5} \quad [6]$$

where the number of grains, N_i, in each ith grain size, D_i, was calculated under each annealing condition from EBSD data. Figure 15(a) shows the relationship between the experimental (mean and standard deviation) and calculated size of the DSR-deformed LCS samples under all annealing treatment conditions. Indeed, Figure 15(a) includes the data for the annealing treatment of IF steel samples deformed by ECAP[38] and by a combination of ECAP and cold rolling (ECAP + CR).[39] The computed statistical parameters for ECAP + CR-deformed samples corresponded closely to the values measured over a range of annealing temperatures, suggesting that continuous grain coarsening occurred during annealing. On the other hand, notable deviations from the line shown in Figure 15(a) occurred in the ECAP-deformed samples during annealing at 983 K (710 °C) for more than 180 seconds, as indicated in Figure 15(a), showing discontinuous grain coarsening. The variation between these two results (ECAP and ECAP + CR) was explained based on the fraction of deformation-induced HABs. Therefore, the high fraction of HABs was achieved in the IF steel samples after ECAP + CR deformation (~80 pct) resulted in continuous grain coarsening. Since the mobility and the energy of the high-angle boundaries are not strong functions of boundary misorientations,[47] the high fraction of HABs achieved after ECAP + CR (~80 pct) resulted in microstructures with high thermal stability (continuous grain coarsening).

Under the present annealing conditions, homogeneous softening occurred in the ferrite phase without a discernible nucleation and growth sequence, indicating a mechanism of continuous grain coarsening. The subsequent homogeneous evolution of the microstructure during annealing of the DSR-deformed LCS samples (continuous grain coarsening) coupled with no significant appreciable change in texture was consistent with the later stages of continuous recrystallization involving a gradual increase in grain size by general boundary migration. The fraction HABs provides a suitable method for identifying the nature of the recrystallization process that occurs during annealing. Jazaeri and Humphreys[44] reported that the sharp increase in the fraction of HABs during annealing indicates the occurrence of discontinuous recrystallization, which was verified by a comparison with standard methods of
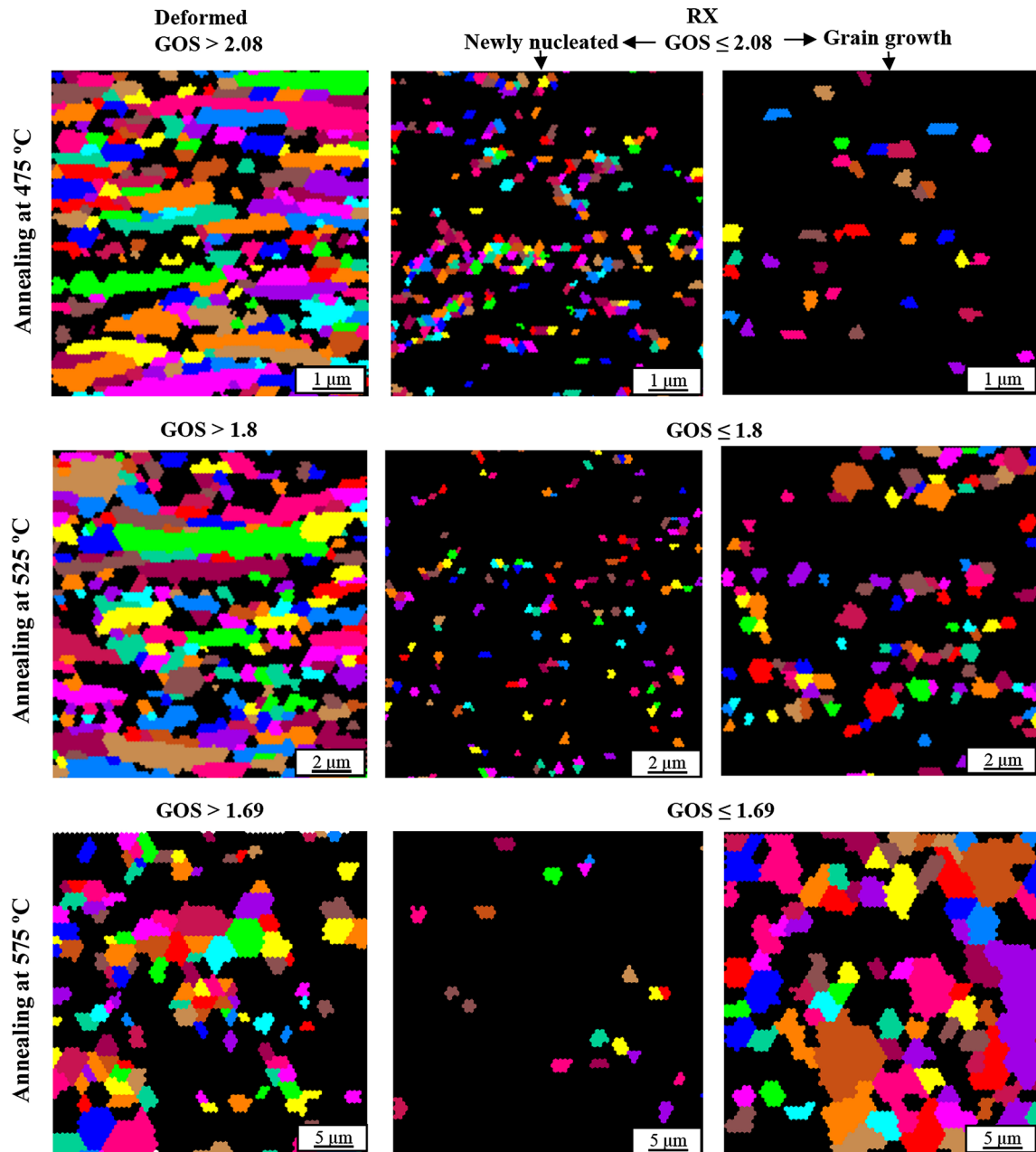
Fig. 12—EBSD maps of the partitioned RX and deformed microstructures for the DSR-deformed LCS samples after isochronal annealing for 1 h at 748 K, 798 K, and 848 K (475 °C, 525 °C, and 575 °C).

assessing discontinuous recrystallization. On the other hand, the fraction of HABs remained relatively unchanged when continuous recrystallization occurred. In the present DSR-deformed LCS samples, the fraction of HABs increased slightly with increasing annealing temperature, suggesting continuous recrystallization, as shown in Figure 15(b). In this case, the subgrains formed after deformation by DSR grew during annealing and the subgrain boundaries area decreased, leading to the formation of high-angle grain boundaries. The occurrence of continuous recrystallization was also reported during the annealing of LCS (0.22 wt pct C) with ultrafine ferrite grains fabricated by a large-strain warm deformation.[45] The fraction of HABs in the as-deformed samples (~62 pct) changed slightly after annealing at 823 K (550 °C) for 2 hours (~65 pct), as shown in Figure 15(b). Good similarity between these two cases was observed, where the fractions of HABs in the as-deformed materials were greater than 60 pct. On the other hand, the ECAP-deformed IF steel samples, with ~63 pct HABs, exhibited discontinuous recrystallization behavior, as shown in Figure 15(b). Although the fractions of deformation-induced HABs in the IF steel samples (ECAP deformation) and the present LCS samples were similar, the different recrystallization behaviors were observed during annealing. From the
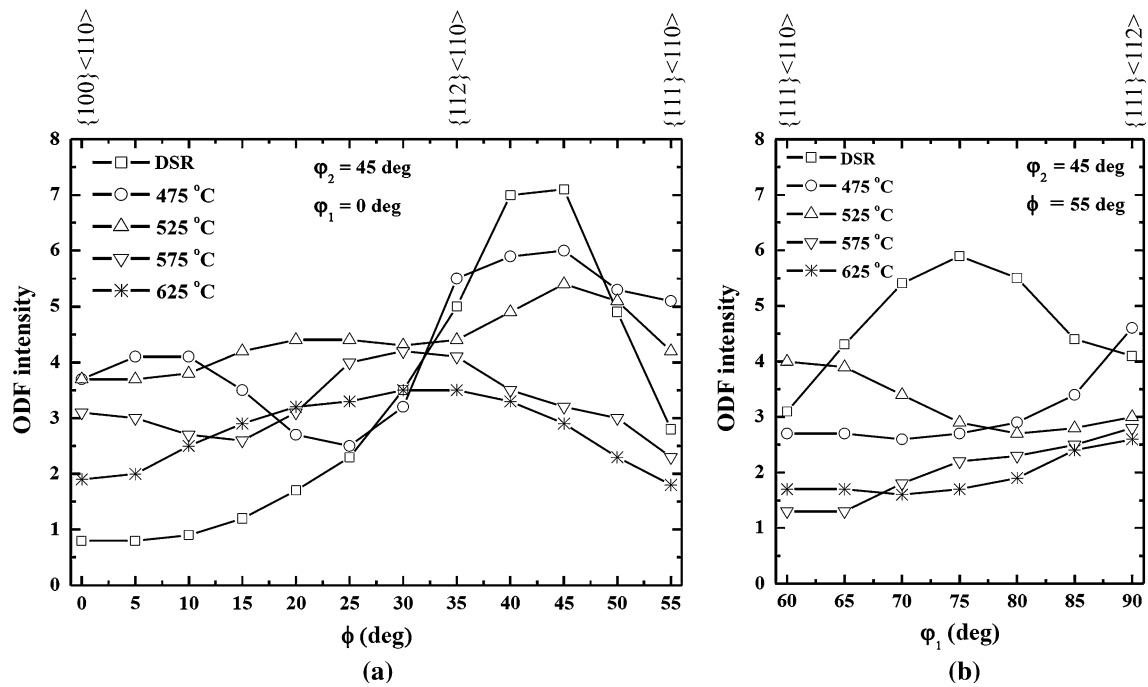
Fig. 13—Intensity distributions of the DSR-deformed LCS samples after isochronal annealing for 1 h along (a) α-fiber and (b) γ-fiber.
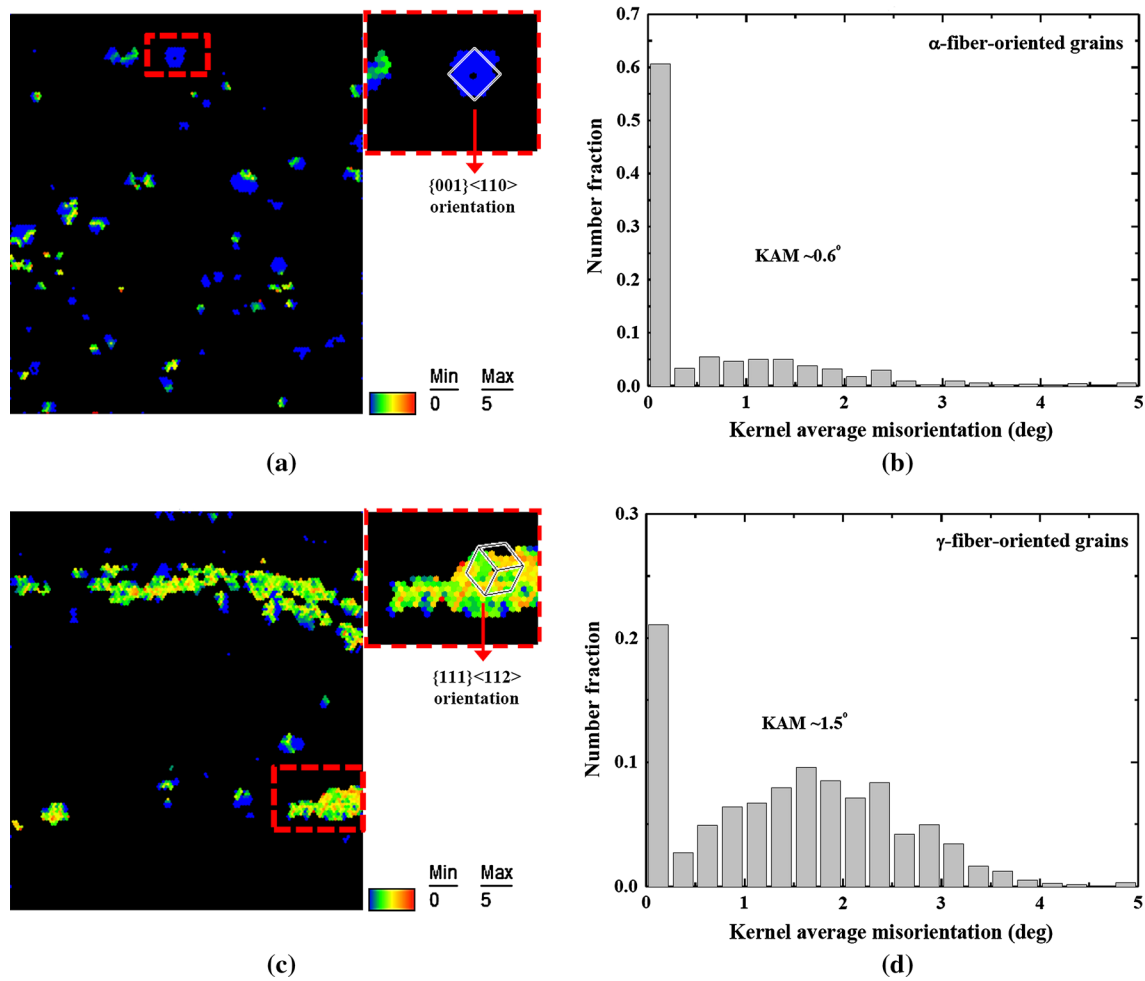

Fig. 14—Kernel average misorientations (KAM) maps and distributions of (a) and (b) α-fiber-oriented grains, (c) and (d) γ-fiber-oriented grains.
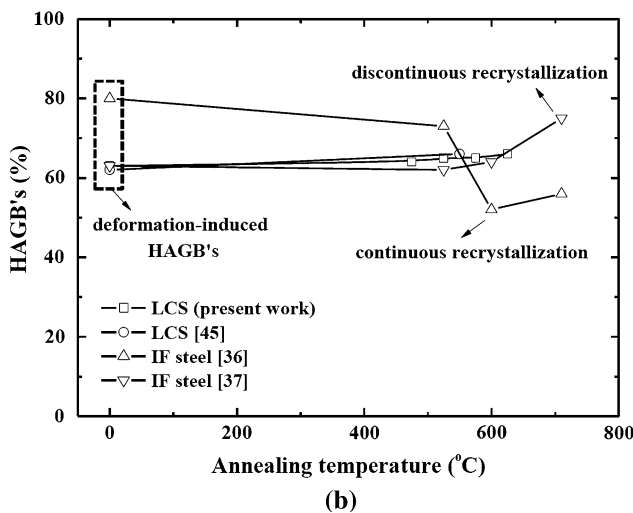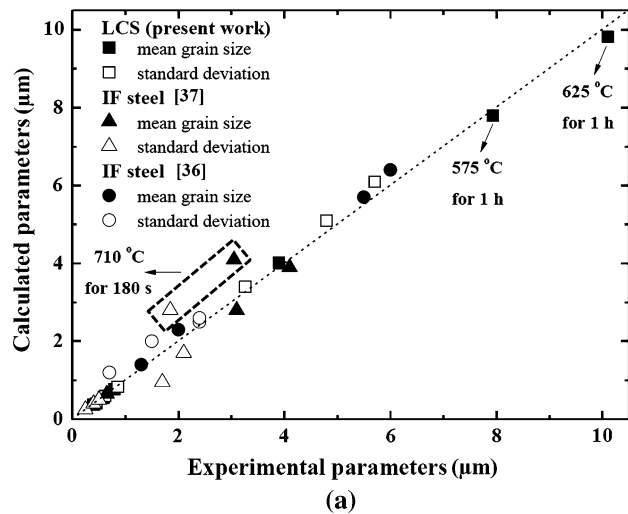
Fig. 15—(a) Relationship between the measured arithmetic mean grain size and standard deviation with the calculated parameters generated from the fitted lognormal distributions under several annealing conditions and processed materials. (b) Fraction of high-angle boundaries (HABs) of several materials as function of the annealing temperature.

data presented in Figure 15(b) for different steel materials, continuous recrystallization occurred in both the single-phase and multi-phase alloys, which was promoted by the fraction of deformation-induced HABs, in the case of the ECAP + CR-deformed IF steel samples. A comparison of the recrystallization behaviors in the steel materials shown in Figure 15(b) indicates that continuous recrystallization was also promoted by the presence of the pearlite colony. Generally, after the SPD deformation of LCS materials, with ferrite and pearlite, the pearlitic cementite lamellae is spheroidized, resulting in a fine distribution of cementite in the microstructure. According to Zener pinning,[47] a fine distribution of cementite can lead to a high dragging force for the migration of grain boundaries, inhibiting the occurrence of discontinuous recrystallization.

V. CONCLUSIONS

The annealing behavior of ultrafine-grained 0.18 wt pct carbon steel samples fabricated by a differential speed rolling (DSR) process was investigated at temperatures between 698 K and 898 K (425 °C and 625 °C) for 1 hour. Deformation by the DSR process at room temperature resulted in a complex microstructure in the ferrite phase consisting of an equiaxed structure with a mean grain size of ~0.4 μm and a lamellar structure with a mean lamellar width of ~0.35 μm. The textures evolved in the LCS sample after 4-pass DSR deformation consisted of components with orientations belonging to the rolling texture and shear texture. During heat treatment at 748 K (475 °C) for 1 hour after DSR deformation, an ultrafine-grained microstructure with a ferrite grain size of ~0.8 μm was obtained. The grain boundary misorientations of the ultrafine ferrite grains were evaluated quantitatively, and ~67 pct of the boundaries were found to be high-angled boundaries. The extremely fine new ferrite grains with a size less than ~0.1 μm appeared near the grain boundaries after annealing 798 K (525 °C) suggesting that the recovery was almost complete, and recrystallization became active after annealing at 798 K (525 °C). After annealing at 748 K (475 °C) for 1 hour, the strong fiber textures consisting of α-fibers and γ-fibers, which were formed after deformation by DSR, tended to become more uniform. This tendency became more pronounced with increasing annealing temperature. Continuous coarsening during annealing of the DSR-deformed LCS samples, coupled with no significant appreciable change in texture, indicated the later stages of continuous recrystallization.

REFERENCE

1. R.Z. Valiev, R.K. Islamgaliev, and I.V. Alexandrov: *Prog. Mater. Sci*, 2000, vol. 45, pp. 103–89.
2. Y.G. Ko, D.H. Shin, K.T. Park, and C.S. Lee: *Scripta Mater.*, 2006, vol. 54, pp. 1785–89.
3. O. Saray, G. Purcek, I. Karaman, T. Neindorf, and HJ Maier: *Mater. Sci. Eng.*, 2011, vol. A528, pp. 6573–83.
4. Y.G. Ko, C.S. Lee, D.H. Shin, and S.L. Semiatin: *Metall. Mater. Trans. A*, 2006, vol. 37A, pp. 381–91.
5. C. Xu, S. Schroeder, P.B. Berbon, and T.G. Langdon: *Acta Mater.*, 2010, vol. 58, pp. 1379–86.
6. F.H. Latief and S.I. Hong: *Met. Mater. Int.*, 2015, vol. 19, pp. 746–52.
7. A.P. Zhilyaev and T.G. Langdon: *Prog. Mater. Sci.*, 2008, vol. 53, pp. 893–979.
8. N. Tsuji, Y. Saito, S.H. Lee, and Y. Minamino: *Adv. Eng. Mater.*, 2003, vol. 5, pp. 338–44.

9. X. Huang, K. Suzuki, A. Watazu, I. Shigematsu, and N. Saito: *J. Alloys Compd.*, 2008, vol. 457, pp. 408–12.
10. W.J. Kim, B.G. Hwang, M.J. Lee, and Y.B. Park: *J. Alloys Compd.*, 2011, vol. 509, pp. 8510–17.
11. T.G. Langdon: *Mater. Sci. Eng. A*, 2007, vol. 462, pp. 3–11.
12. Y.H. Kim and W.J. Kim: *Met. Mater. Int.*, 2015, vol. 21, pp. 374–81.
13. W.J. Kim, J.B. Lee, W.Y. Kim, H.T. Jeong, and H.G. Jeong: *Scripta Mater.*, 2007, vol. 56, pp. 309–12.
14. H. Watanabe, T. Mukai, and K. Ishikawa: *J. Mater. Process. Technol.*, 2007, vol. 182, pp. 644–47.
15. Loorentz and Y.G. Ko: *J. Alloys Compd.*, 2012, vol. 536S, pp. S122–25.
16. Loorentz and Y.G. Ko: *J. Alloys Compd.*, 2014, vol. 586S, pp. S205–09.
17. S.H. Lee, S.R. Lee, and H. Utsunomiya: *Korean J. Met. Mater.*, 2014, vol. 52, pp. 637–47.
18. W.J. Kim, K.E. Lee, and S.H. Choi: *Mater. Sci. Eng. A*, 2009, vol. 506, pp. 71–79.
19. W. Polkowski, P. Jozwik, M. Polanski, and Z. Bojar: *Mater. Sci. Eng. A*, 2013, vol. 564, pp. 289–97.
20. W.J. Kim, S.J. Yoo, and J.B. Lee: *Scripta Mater.*, 2010, vol. 62, pp. 451–54.
21. X. Huang, K. Suzuki, and Y. Chino: *Scripta Mater.*, 2010, vol. 64, pp. 473–76.
22. J.S. Kim, S. Kim, and S.H. Choi: *Korean J. Met. Mater.*, 2014, vol. 52, pp. 361–72.
23. Y.G. Ko, J. Suharto, J.S. Lee, B.H. Park, and D.H. Shin: *Met. Mater. Int.*, 2013, vol. 19, pp. 603–09.
24. Y.G. Ko, J.S. Lee, and Loorentz: *Mater. Sci. Tech.*, 2013, vol. 29, pp. 553–58.
25. K. Hamad, R.B. Megantoro, and Y.G. Ko: *J. Mater. Sci.*, 2014, vol. 49, pp. 6608–19.
26. K. Hamad, B.K. Chung, and Y.G. Ko: *Mater. Charact.*, 2014, vol. 94, pp. 203–14.
27. W. Polkowski, P. Jozwik, and Z. Bojar: *Metall. Mater. Trans. A*, 2015, vol. 46, pp. 2216–26.
28. K.T. Parka and D.H. Shin: *Mater. Sci. Eng. A*, 2002, vol. 334, pp. 79–86.
29. G.G. Maier, E.G. Astafurova, H.J. Maier, E.V. Naydenkin, G.I. Raab, P.D. Odessky, and S.V. Dobatkine: *Mater. Sci. Eng. A*, 2012, vol. 581, pp. 104–07.
30. D.A. Hughes and N. Hansen: *Acta Mater.*, 1997, vol. 45, pp. 3871–86.
31. N. Kamikawa, T. Sakai, and N. Tsuji: *Acta Mater.*, 2007, vol. 55, pp. 5873–88.
32. E. Bonnot, A. Helbert, F. Brisset, and T. Baudin: *Mater. Sci. Eng. A*, 2013, vol. 561, pp. 60–66.
33. D. Raabe: *Acta Mater.*, 1997, vol. 45, pp. 1137–51.
34. S. Chen, J. Butler, and S. Melzer: *J. Magn. Magn. Mater.*, 2014, vol. 368, pp. 342–52.
35. M. Ferry and N. Burhan: *Acta Mater.*, 2007, vol. 55, pp. 3479–91.
36. S.S. Hazra, E.V. Pereloma, and A.A. Gazder: *Mater. Sci. Eng. A*, 2011, vol. 530, pp. 492–503.
37. S.S. Hazra1, E.V. Pereloma and A.A. Gazder: *Acta Mater.*, 2011, vol. 59, pp. 4015–29.
38. A.A. Gazder, M. Araiza, J. Jonas, and E.V. Pereloma: *Acta Mater.*, 2011, vol. 59, pp. 4847–65.
39. A.A. Gazder, V.Q. Vu, A.A. Saleh, P.E. Markovsky, O.M. Ivasishin, C.H.J. Davies, and E.V. Pereloma: *J. Alloys Compd.*, 2014, vol. 585, pp. 245–59.
40. F.J. Humphreys and M. Hatherly: *Recrystallization and Related Annealing Phenomena*, Pergamon Press, Oxford, 2004.
41. S. Mandal, S.K. Mishra, A. Kumar, I. Samajdar, P.V. Sivaprasad, T. Jayakumar, and B. Raj: *Phil. Mag.*, 2008, vol. 88, pp. 883–97.
42. Y. Cao, H. Di, J. Zhang, J. Zhang, T. Ma, and R.D.K. Misra: *Mater. Sci. Eng. A*, 2013, vol. 585, pp. 71–85.
43. S. Biswas, D. Kim, and S. Suwas: *Mater. Sci. Eng. A*, 2012, vol. 550, pp. 19–30.
44. H. Jazaeri and F.J. Humphreys: *Acta Mater.*, 2004, vol. 52, pp. 3251–62.
45. R. Song, D. Ponge, D. Raabe, and R. Kaspar: *Acta Mater.*, 2005, vol. 53, pp. 845–58.
46. L. Storojeva, D. Ponge, R. Kaspar, and D. Raabe: *Acta Mater.*, 2004, vol. 52, pp. 2209–20.
47. R.D. Doherty, D.A. Hughes, F.J. Humphreys, J.J. Jonas, D.Juul Jensen, M.E. Kassner, W.E. King, T.R. McNelley, H.J. McQueen and A.D.: *Mater. Sci. Eng.* 1997, vol. A238, pp. 219–428.